



Numerical prediction of in-plane permeability for multilayer woven fabrics with manufacture-induced deformation



Xuesen Zeng*, Andreas Endruweit, Louise P. Brown, Andrew C. Long

Faculty of Engineering, Division of Materials, Mechanics & Structures, University of Nottingham, University Park, Nottingham NG7 2RD, UK

ARTICLE INFO

Article history:
Available online 4 April 2015

Keywords:

A. Fabrics/textiles
C. Computational modelling
E. Resin flow

ABSTRACT

A unit cell based Computational Fluid Dynamics model is presented for predicting permeability of multilayer fabric structures. In Liquid Composites Moulding processes, fabric lay-ups undergo significant manufacture-induced deformation, combining compression, shear, and inter-layer nesting. Starting from the configuration of un-deformed fabric, the deformation is simulated geometrically by accounting for self-imposed kinematic constraints of interweaving yarns. The geometrical modelling approach is implemented in the open-source software TexGen. The permeability tensor is retrieved from flow analysis in ANSYS/CFX, based on TexGen voxel models. Using only measured geometrical data for un-deformed fabrics, deformed plain weave fabric and twill weave fabric lay-ups were modelled and their permeability tensors predicted. Comparison with experimental data demonstrates the generally good accuracy of predictions derived from the proposed numerical method.

© 2015 The Authors. Published by Elsevier Ltd. This is an open access article under the CC BY license (<http://creativecommons.org/licenses/by/4.0/>).

1. Introduction

During preforming for Liquid Composite Moulding (LCM) processes, lay-ups of woven reinforcement fabric are subject to a combination of shear, compression and nesting. Previous studies have shown that the fabric permeability, which determines the subsequent impregnation with a liquid resin system, is highly sensitive to deformations of the fabric architecture due to shear [1–6], compression [7–9], nesting [10–12], and material handling history [13].

Experimentally determined fabric permeability data often show significant scatter and appear to depend on the experimental protocol, which was the focus of two recent international benchmark exercises [14,15]. The second benchmark exercise [15] confirmed that set-up and execution of experiments have an effect on measured permeabilities. Predictive permeability modelling has the potential to eliminate human errors, which occur in setting up and conducting experiments and may affect permeability data, provided that a suitable modelling approach is chosen.

In the literature, meso–macro approaches are proposed to describe the permeability as a function of the fibre volume fraction and the shear angle [1–5]. Since details of the actual fabric structure are typically ignored, they need to be calibrated with experimental permeability values and are not truly predictive.

A number of numerical meso-scale modelling approaches for fabric permeability are documented in the literature [6,16–21]. In some of these studies, the geometry of woven fabrics is idealized by assuming constant yarn cross-section and sinusoidal/zig-zag yarn paths. Consequently, the simplification in describing woven yarn geometries results in large differences between model predictions and experimental data, or the predictions remained un-validated. Other studies employ textile mechanics to predict realistic yarn geometries [6,19]. This requires mechanical properties of the textile, including shear and bending properties, to be characterised as input.

This study proposes a modelling approach, which is based on geometrical data and self-imposed kinematic constraints of interweaving yarns, to simulate woven fabric structures under realistic manufacturing conditions. The implementation is automated in the open source software TexGen [22,23] for generation of geometrical textile models. The commercial code ANSYS/CFX is employed for Computational Fluid Dynamics (CFD) analysis of impregnating flow through the generated fabric geometries as a pre-requisite for fabric permeability determination. The approach is evaluated for two woven fabric lay-ups at controlled compression and/or shear deformation.

2. Geometrical modelling of fabric lay-ups

In a first step, realistic geometrical modelling is applied to single fabric layers. Moderate deformation of fabrics includes effects

* Corresponding author.

E-mail address: xuesen.zeng@nottingham.ac.uk (X. Zeng).

such as shear before reaching the locking angle and/or through-thickness compression of fabric lay-ups at low compaction pressure. In these cases, no excessive distortion of the fibre architecture occurs. The fabric geometry mainly undergoes kinematic changes, i.e. (1) re-orientation of yarn paths; (2) local rotation of yarn cross-sections around the yarn axis; (3) change of local yarn cross-sectional shapes. The deformation is simulated based on a purely geometrical modelling approach, not considering the actual yarn mechanics. For realistic modelling, basic geometrical considerations imply that the major axis of a rotated (elliptical) yarn cross-section is parallel to the tangent at the contact between two non-parallel (crossing) yarns. Artificial yarn intersections in the geometrical model are avoided through local adaptation of the yarn cross-sectional shape, which is applied automatically in TexGen and is based on conservation of the total yarn volume.

2.1. Fabric shear

Two identical idealised yarns, which were initially perpendicular and are now sheared by an angle γ , such that yarn II is now oriented at an angle $(90^\circ - \gamma)$ relative to yarn I, are shown in Fig. 1(a) prior to any local rotation of yarn cross-sections around the yarn axis. The local rotational angle, β , of the yarn cross-section of yarn II depends on the yarn cross-sectional width, w , yarn cross-sectional height, h , shear angle, γ , and nominal position, R , of the contact point. The normalised coordinate, R , with $0 < R < 1$ refers to a point on the segment of the axis of yarn II, where it crosses over yarn I (Fig. 1(a)). The sectional view A–A in Fig. 1(b), after applying the local rotation of yarn II around its axis, illustrates the tangential relationship of two elliptical cross-sections which determines the rotational angle, β . With the width $w' = w/\sin \gamma$, the parametric equations of the cross-section of yarn I in the A–A view are

$$x = \frac{w'}{2} \cos t = \frac{w}{2 \sin \gamma} \cos t \text{ and } y = \frac{h}{2} \sin t, \tag{1}$$

where t is the eccentricity parameter ($0 \leq t \leq 2\pi$).

When the nominal contact point, at position R in Fig. 1(a), is projected along the y -axis in the A–A view, prior to cross-sectional rotation, onto the cross-section of yarn I, the projected point, $(x(T), y(T))$, is the actual contact point between cross-section I and II. Here, T is the eccentricity parameter of the contact point in the A–A section, which is related to R through

$$R = \frac{w'/2 - x(T)}{w'} = 0.5 - 0.5 \cos T, \tag{2}$$

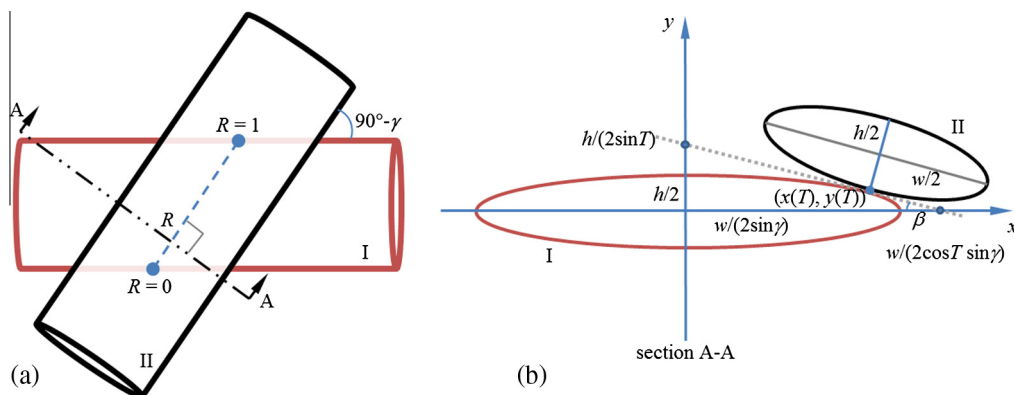


Fig. 1. (a) Two identical elliptical cylinders, I and II, crossing over each other; (b) surface tangent between two ellipses at sectional view A–A of (a). (For interpretation of the references to colour in this figure legend, the reader is referred to the web version of this article.)

or

$$\cos T = 1 - 2R. \tag{3}$$

The tangent to the elliptical cross-sections at the contact point intersects the x - and y -axes at the points $(w/(2\cos T \sin \gamma), 0)$ and $(0, h/(2\sin T))$, respectively (Fig. 1(b)). These two intersection points are then used to calculate the local rotation angle, β , for the cross-section of yarn II. Local rotation angles are calculated for R varying from 0 to 1.

Based on the idealised derivation above, the tangential angle, β , would be approximately 90° at contact points near $R = 0$ and $R = 1$. This would introduce an unrealistic local rotation of the yarn cross-section. Hence, to avoid the extreme 90° rotation, the rotational angle is calculated by offsetting the contact point position, R . Implementation of the offset scheme in TexGen allows realistic local yarn rotations at varying contact points ($0 < R < 1$) to be captured and values for β near 90° to be avoided near $R = 0$ and $R = 1$ (Fig. 2). The following offset scheme is applied in TexGen

$$R' = \begin{cases} R + \frac{1}{10} \sin \gamma & \text{if } 0.0 \leq R < 0.5 \\ R - \frac{1}{10} \sin \gamma & \text{if } 0.5 < R \leq 1.0 \end{cases} \tag{4}$$

The offset, $1/10 \sin \gamma$, reflects the finite compliance of yarn II in conforming to the surface of yarn I. Based on the assessment of TexGen model for a range of offset values, the factor, $1/10$, was found to give plausible results in terms of yarn curvature for a wide range of yarn cross-sectional shapes. The discontinuity at $R = 0.5$ in Eq. (4) is avoided through interpolation of the yarn path based on 20 discrete data points sampled by TexGen. With severe inter-yarn intersections being avoided in a unit cell model, the procedure of applying local yarn rotation (Eqs. 1–4) effectively represents the main yarn geometry changes during shear of a woven fabric.

2.2. Yarn cross-section variation under shear and compaction

Rotation of the yarn cross-section (Section 2.1) prevents severe intersection of yarns at the cross-over point, illustrated in Fig. 3(a) and (b). For any remaining interference between yarns, further changes are made to the yarn cross-sectional shape: When intersections between a yarn cross-section and an adjacent yarn are detected, the positions of points on the cross-section are adjusted, replacing the originally elliptical cross-section with a polygon. The resulting yarn geometry is shown in Fig. 3(c).

It has been observed experimentally that in compaction of fabric lay-ups, yarns tend to flatten, and there is an offset between the axis of one yarn and the point at which the yarn passing over it drops away (Fig. 4). In order to simulate the geometrical features presented in Fig. 4, an algorithm has been developed which allows

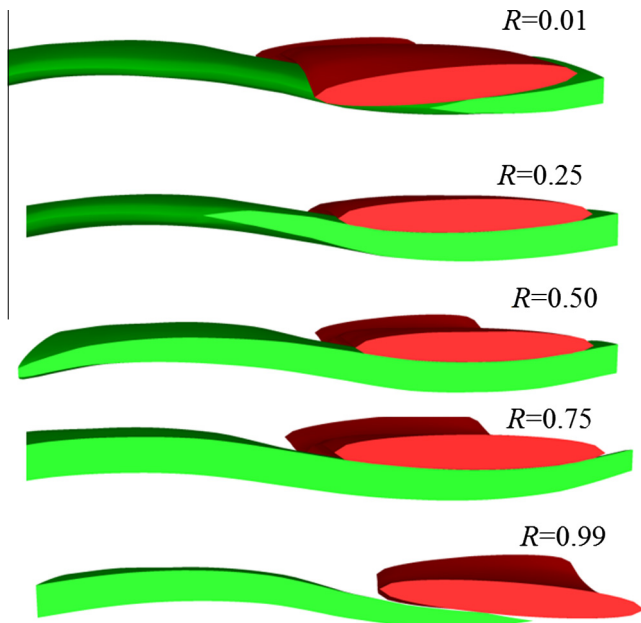


Fig. 2. Predicted yarn rotations along the axis of the top yarn (different values of R) in a TexGen model. (For interpretation of the references to colour in this figure legend, the reader is referred to the web version of this article.)

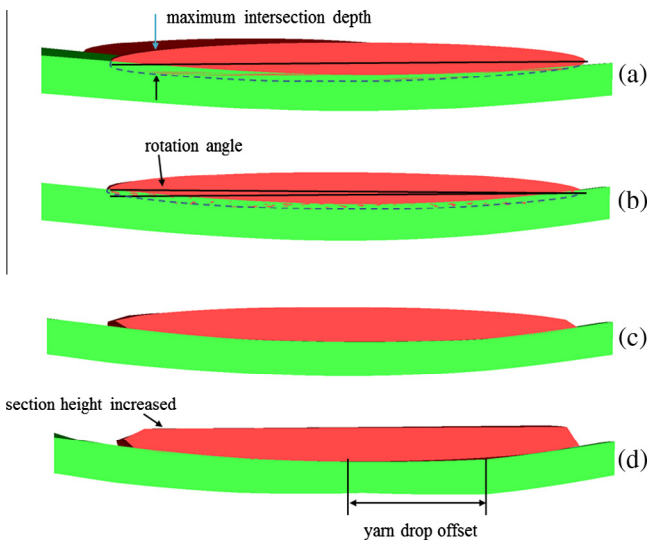


Fig. 3. Geometrical refinement stages: (a) unrefined; (b) rotation only; (c) rotation and intersection correction; (d) rotation, intersection correction and adjusted section height. (For interpretation of the references to colour in this figure legend, the reader is referred to the web version of this article.)

the yarn cross-sectional shape to be varied along the yarn axis. It is assumed that each yarn is bound between two parallel planes at a distance corresponding to the specified fabric thickness (Fig. 5). For each cross-section, the nearest distances between points on the yarn perimeter and either the upper or lower bounding plane, $\Delta\tau$, are identified. If $\Delta\tau < 0$ for any point on the yarn perimeter, there are intersections of the yarn with the nearest bounding plane. The yarn cross-sectional shape is corrected by moving the points until the respective values of $\Delta\tau$ are zero, thus constraining the yarn to the specified fabric thickness. For points on the yarn perimeter with initial values $\Delta\tau > 0$, the position is adjusted using an iterative method to restore the original cross-sectional area whilst being bound within the planes. Fig. 3(d) shows the final stage of the refinement, where the height of the upper yarn is increased until

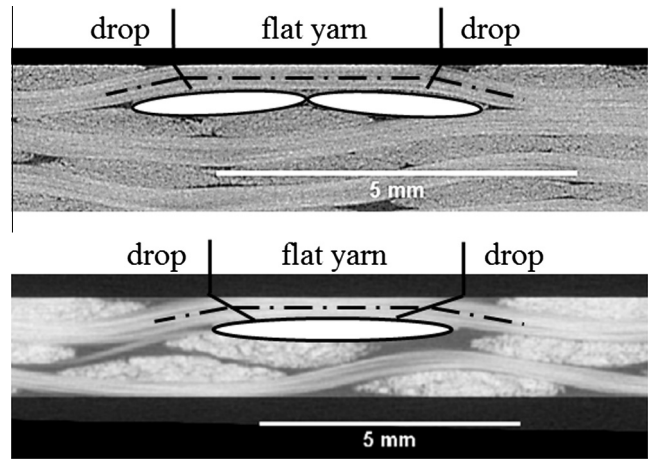


Fig. 4. Yarn drop offset under compression in twill weave fabric (top) and plain weave fabric (bottom).

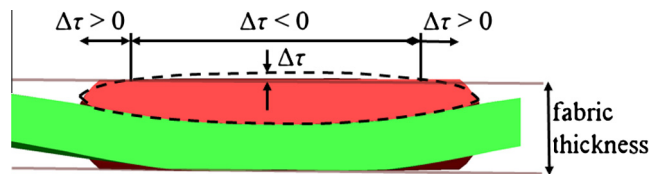


Fig. 5. Intersection of yarn cross-section with bounding planes for fabric thickness, with penalty, $\Delta\tau$. The dashed line indicates the initial shape whilst the solid colour is the final shape after applying $\Delta\tau$. (For interpretation of the references to colour in this figure legend, the reader is referred to the web version of this article.)

it reaches the limit determined by the overall fabric thickness. The side view of the lower yarn shows the yarn drop offset produced by the height adjustment at different sections along the yarn.

Based on the refinement approach above, cross-sections along the path of a single yarn vary systematically depending on the interweaving geometrical constraints. Fig. 6 compares simulated yarn cross-sectional variations with those in the real material. The figure suggests that, despite the simplifications in the modelling process, the main features of real yarn cross-sections, such as asymmetry, varying aspect ratio, and distinct tips, are reproduced in the model.

2.3. Fabric lay-up

Previous studies have highlighted the influence of nesting in multilayer reinforcements on permeability scatter [11,12]. Nesting involves complex interactions between fabric layers leading to layer thickness changes and localised compaction. Since the interdependence between in-plane layer shift and through-thickness compaction cannot be modelled accurately, the effect of nesting on the formation of gap spaces in the lay-up is approximated in two stages. In the first stage, each individual fabric layer undergoes compaction between two (virtual) flat mould surfaces, the spacing of which corresponds to the average layer thickness. In the second stage, multiple (identical) layers of the compacted flat fabric are stacked on top of each other, and in-plane shifting in the warp and weft direction is applied. Although this approach does not capture the precise interaction between layer shift and local compaction, it reflects the approximate geometry and connectivity of flow channels in between fabric layers at given global fibre volume fraction.

Latin hypercube sampling [24] was employed to generate in-plane shift vectors. Compared to generic Monte-Carlo sampling,

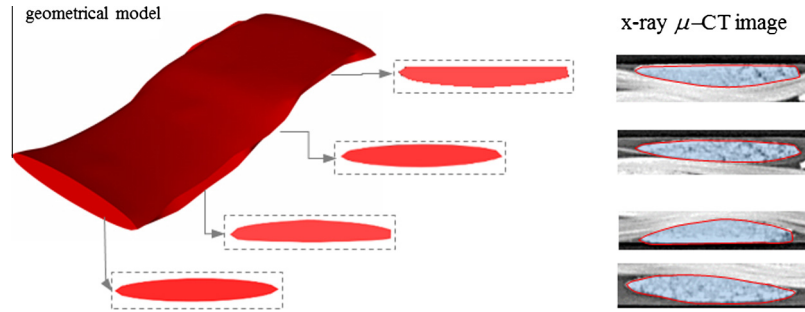


Fig. 6. Yarn cross-sectional details in an automatically generated geometrical model, representing typical features found in X-ray μ -CT scans of the corresponding plain weave fabric laminate composites. (For interpretation of the references to colour in this figure legend, the reader is referred to the web version of this article.)

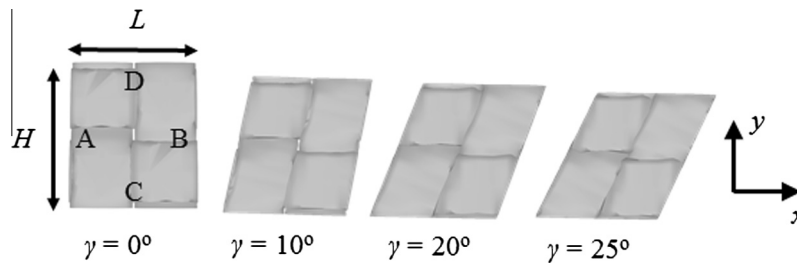


Fig. 7. Automatically generated unit cell models with shear angles of 0°, 10°, 20° and 25° relative to the y -axis.

Latin hypercube sampling produces more evenly distributed samples from the entire ranges of the variables, thus allowing to fully explore multi-dimensional inputs based on limited numbers of simulations [25,26]. The Latin hypercube design function $X = \text{lhsdesign}(N, P)$ from MatLab – Release 2013 was used, which generates a sample X containing N values on each of P variables.

2.4. Automation of unit cell generation

The modelling approach described in Sections 2.1–2.3 is implemented and automated as a 2D fabric wizard in TexGen. Fig. 7 illustrates unit cell models of a single ply of a plain weave fabric at various shear angles. Fig. 8 shows two lay-up models, 3 layers of a sheared plain weave fabric and 9 layers of a twill weave fabric. The unit cell domain is defined as shown in Fig. 8 to ensure the translational periodicity for each fabric layer at any shear angle and in-plane shift. Periodicity is utilized later in the CFD analysis described in Section 3. The geometrical unit cell models are discretised into voxels and converted to input files for flow analysis in ANSYS/CFX.

3. CFD analysis for permeability prediction

The meshed CFD models comprise yarns and the surrounding empty spaces in the mould cavity for resin injection. The permeabilities of yarns, which can be estimated based on the models proposed by Gebart [27], assuming ideal square or hexagonal filament arrangement, are typically two orders smaller than the overall permeabilities of the fabric lay-ups. Thus, the yarns can be assumed to be impermeable which helps to reduce the computational cost for CFD simulations. This assumption was validated numerically by Nedanov and Advani [16]. Steady-state flow through the pore spaces was simulated. Translational periodic boundary conditions were applied on opposite faces of the textile unit cell domain in weft and warp directions to represent a continuous reinforcement. A flow-driving pressure drop was applied in either warp or weft direction. Non-slip wall boundary conditions were specified at the top and bottom faces of the domain to

simulate flow along the mould surfaces during in-plane fabric impregnation. Since inter-yarn gap spaces are typically two orders larger than pore spaces in the yarns, lubrication at the yarn-gap interface can be assumed to be negligible, based on the study by Groupe and Akkerman [28]. Hence non-slip boundary conditions were also applied on the yarn surfaces. To validate the assumptions for flow modelling, CFD simulations were run for single layers of the two fabrics analysed in this study, where the porosity of yarns was considered, and finite slip was applied on the yarn surfaces. Permeabilities predicted based on the method described in the following differed by less than 1% from corresponding values solid yarns and non-slip boundary conditions.

Darcy's law for a 2D flow problem can be expressed in global x - y coordinates as

$$\begin{pmatrix} u \\ v \end{pmatrix} = \frac{1}{\eta} \begin{pmatrix} K_{xx} & K_{xy} \\ K_{yx} & K_{yy} \end{pmatrix} \begin{pmatrix} \partial p / \partial x \\ \partial p / \partial y \end{pmatrix}, \quad (5)$$

where u and v are the flow velocity components, K_{xx} , K_{yy} , and $K_{xy} = K_{yx}$ are the components of the permeability tensor to be determined by unit cell based CFD analysis, p is the fluid pressure, and η is the fluid viscosity. For a sheared unit cell domain, translational periodic boundary conditions are applied on the pairs of face A/face B and face C/face D (Fig. 7). From each CFD simulation, a flow velocity vector is calculated on faces A, B, C and D as averaged nodal velocity weighted by the area of the respective face. The permeability tensor in Eq. (5) is determined based on two flow cases.

In case I, a pressure drop, Δp , is imposed between face C and face D (the distance between which is H), such that $\partial p / \partial x = 0$ and $\partial p / \partial y \approx \Delta p / H$. With the resulting velocity components, u_1 and v_1 , Eq. (5) can be solved:

$$K_{xy} = K_{yx} = \frac{u_1 \eta H}{\Delta p}; \quad K_{yy} = \frac{v_1 \eta H}{\Delta p} \quad (6)$$

In case II, a pressure drop, Δp , is imposed between face A and face B (the distance between which along the x direction is L), such that $\partial p / \partial x \approx \Delta p / L$ and $\partial p / \partial y \approx \Delta p / (L \tan \gamma)$, where γ is the shear angle. With u_2 , v_2 and Eq. (5):

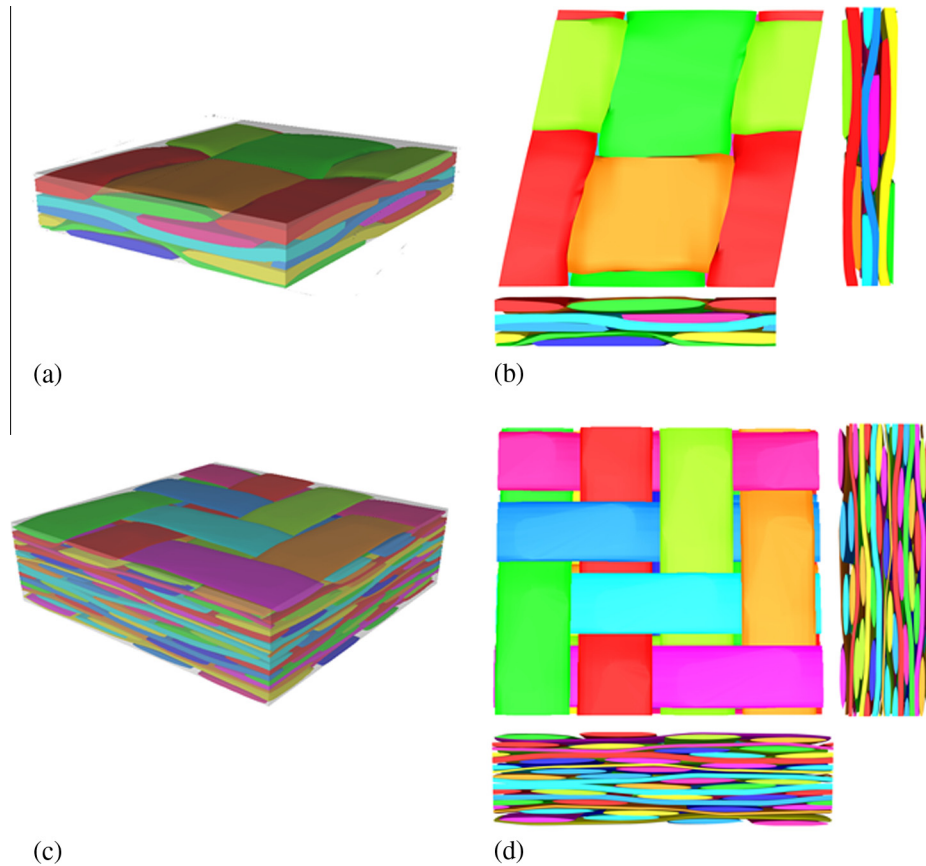


Fig. 8. (a) and (b) Unit cell model of 3 layers of a plain weave fabric sheared to $\gamma = 10^\circ$; (c) and (d) unit cell model of 9 layers of a twill weave fabric at $\gamma = 0^\circ$. (For interpretation of the references to colour in this figure legend, the reader is referred to the web version of this article.)

$$K_{xx} = \frac{\eta L}{\Delta p} \left(u_2 - \frac{H \tan \gamma}{L} u_1 \right) \quad (7)$$

The permeability tensor is then transformed to the diagonal form (K_1 and K_2) [29], to allow direct comparison with experimental data.

4. Materials and permeability measurement

4.1. Materials

A 2×2 twill weave carbon fibre fabric (with a nominal areal density $S_0 = 285 \text{ g/m}^2$ and filament count $c_f = 6 \text{ K}$) and a plain weave glass fibre fabric (with $S_0 = 895 \text{ g/m}^2$) were selected for validating the numerical approach for permeability prediction. The two fabrics differ in weave style and areal density, which leads to distinctive features in meso-scale yarn geometry, as shown in Fig. 9. These image data were acquired from two sources: (a) 3D X-ray micro-Computed Tomography (μ -CT) using a GE Phoenix Nanotom 180NF system and (b) 2D flatbed document scanner. The μ -CT image data offer three-dimensional spatial information on the fabric geometry. However, the size of the scan volume needs to be limited in order to allow high resolution image data to be acquired. For example, the composite specimen with 9 layers of twill weave fabric was scanned in dimensions of $12 \text{ mm} \times 12 \text{ mm} \times 3.5 \text{ mm}$ at a resolution of $6.75 \text{ }\mu\text{m/voxel}$, whilst the specimen with 3 layers of the plain weave fabric was scanned at $30 \text{ mm} \times 30 \text{ mm} \times 2 \text{ mm}$ with a resolution of $20 \text{ }\mu\text{m/voxel}$.

To assess the statistical variability of woven fabric geometry over a large number of weave repeats [30,31], complementary to μ -CT data, 2D images were acquired using the flatbed scanner

providing a large surface view of the fabric ($210 \text{ mm} \times 297 \text{ mm}$) at a resolution of $21.17 \text{ }\mu\text{m/pixel}$. This enables statistically robust measurement of yarn width and yarn spacing. To quantify each of these geometrical parameters, 120 measurements were taken. Average values, standard deviations and coefficients of variation are listed in Table 1.

4.2. In-plane permeability measurement

For the 2×2 twill weave fabric, in-plane permeability data were acquired in the framework of the recent permeability benchmark II [15], where use of an experimental set-up for unsaturated linear flow at constant injection pressure was prescribed for permeability characterisation of the unsheared fabric. For the experimental set-up used here, the relative experimental error for each individual experiment, determined by uncertainties in measurement of flow front propagation, fibre volume fraction, fluid viscosity, and applied injection pressure, was quantified as $\pm 7\%$. At a cavity height of 3.5 mm , 9 fabric layers resulted in a fibre volume fraction $V_f = 0.40$.

For the plain weave fabric, the in-plane permeability was measured in unsaturated radial flow experiments at constant injection pressure [32]. Due to the layout of radial injection experiments, sheared fabric specimens can be accommodated. For the set-up used here, the relative experimental error for each individual experiment was $\pm 14\%$. At a cavity height of 2 mm , three fabric layers corresponded to $V_f = 0.51$ for the case of non-sheared fabric ($\gamma = 0^\circ$). Additional permeability measurements were made on 3 layers of the sheared plain weave fabric at a constant cavity height of 2 mm . The resulting fibre volume fractions were $V_f = 0.52$ at a

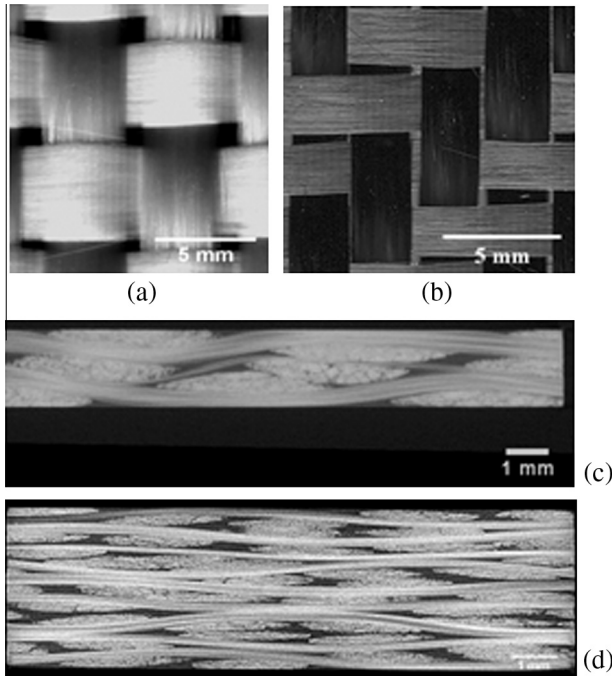


Fig. 9. (a) Glass fibre plain weave fabric; (b) carbon fibre twill fabric; (c) μ -CT image of 3-layer laminate made from the fabric in (a); (d) μ -CT image of 9-layer laminate made from the fabric in (b).

shear angle $\gamma = 10^\circ$, $V_f = 0.55$ at $\gamma = 20^\circ$, and $V_f = 0.56$ at $\gamma = 25^\circ$. The uncertainty in shearing the fabric specimens to given angles before they were placed in the injection tool cavity is estimated as $\pm 5^\circ$.

5. Results and discussions

5.1. Evaluating permeability predictions

In order to compare numerical predictions with experimental measurements (Section 4.2), unit cell models of the tested fabric lay-ups were generated in TexGen using the geometrical data for un-deformed fabrics (2D scans) listed in Table 1 as input. Six stochastic models with varying in-plane layer shift (Section 2.3) were created for each lay-up. To study the mesh sensitivity of CFD analysis based on these models, the following numbers of voxel elements for the unit cell were tested for 9 layers of the twill weave fabric (Fig. 8(c) and (d)): $50 \times 50 \times 90$ (warp \times weft \times thickness), $100 \times 100 \times 180$, $150 \times 150 \times 270$ and $300 \times 300 \times 270$. Convergence of the permeability predictions was found for a mesh with $150 \times 150 \times 270$ voxels. Similarly, for 3 layers of the plain weave fabric (Fig. 8(a) and (b)), results converged for a mesh of $150 \times 150 \times 90$ voxels.

The numerical results for in-plane permeabilities are listed in Table 2 together with the corresponding experimental data. In general, the difference between average values of predicted and experimentally determined permeability is in the same order or smaller than the standard deviation of either value. For the twill

weave fabric lay-up, the predictions of the permeability tensor (K_1 and K_2) deviate on average by 10% from the experimental data. For the plain weave fabric lay-up, the average deviation of the predicted values for K_1 and K_2 from the experimental values is 20% when sheared ($\gamma = 10^\circ$, 20° and 25°). Here, the prediction for the un-sheared plain weave fabric lay-up ($\gamma = 0^\circ$) is an outlier deviating from the experimental data by 150% for K_1 , and by 30% for K_2 .

For this case ($\gamma = 0^\circ$), the interference between yarns is severe, as shown in Fig. 10(a) prior to any refinement. After automated geometrical refinement to correct the interference whilst keeping the fibre volume fraction constant, the resulting model (Fig. 10(b)) has a high degree of resemblance to the real material (Fig. 10(c)). However, the sharp taper of tips in the yarn cross-sections, highlighted with arrows in Fig. 10(b), is recognised as being artificial in comparison with the μ -CT scan. It results from the resolution of cross-sectional modelling in TexGen, which is limited by the number of points defining the yarn perimeter. This geometrical detail introduces additional flow channels in the numerical model for $\gamma = 0^\circ$, leading to enhanced flow in the simulation and over-prediction of the permeability. Nonetheless, Fig. 10(d) shows that the significant difference between predicted and experimental values for K_1 is reduced for models with stochastic layer shift and refined yarn geometry (Fig. 10(b)) compared to stochastic models without any geometrical refinement (Fig. 10(a)).

For the unit cell models of sheared plain weave fabrics, the artificial taper of cross-sectional tips highlighted in Fig. 10(b) is avoided as illustrated in Fig. 2 ($R = 0.25$, 0.50 and 0.75), which is helped mainly by modelling the yarn cross-sectional rotation due to shear (Section 2.1). As a result, the permeability predictions are more accurate for the sheared plain weave fabrics than for the un-sheared fabric.

In general, the numerical predictions achieved higher accuracy for the twill weave fabric lay-up than for the plain weave fabric lay-ups, which can be explained by the higher geometrical complexity in modelling tightly packed woven architectures related to the presence of more geometrical constraints. Since the twill weave fabric ($V_f = 0.40$) has lower fibre volume fraction than the plain weave fabric ($V_f = 0.51$), less surface interference occurs in the geometrical unit cell model prior to any refinement. The lower the degree of surface interference, the more realistic is the geometrical model resulting from the refinement procedure (Section 2), and the more accurate is the permeability prediction.

5.2. Effect of shear on permeability

Numerical predictions of the permeability tensor for the plain weave fabric were obtained as a function of the shear angle, γ . For comparison, a simple analytical model, which was originally proposed by Long et al. [33], Smith et al. [2] and recently applied by Aranda et al. [1], is adapted to relate the in-plane permeability, K_1 and K_2 , to the shear angle, γ . The model is based on a Kozeny–Carman type dependence on the fibre volume fraction and is expressed as

$$\begin{pmatrix} K_1 \\ K_2 \end{pmatrix} = \begin{pmatrix} A_1 \\ A_2 \end{pmatrix} \frac{(1 - V_f)^3}{V_f^2} \cos^2 \left(\frac{90^\circ + \gamma}{2} \right), \quad (8)$$

Table 1

Geometry parameters determined from 3D μ -CT scans of laminates and from 2D scans of single fabric plies: inter-yarn gap width, g , yarn width, w , and yarn height, h , in both fabric directions; average values, standard deviations and coefficients of variation (standard deviation/average) are given where appropriate.

		$g_{\text{weft}}/\text{mm}$	$g_{\text{warp}}/\text{mm}$	$w_{\text{weft}}/\text{mm}$	$h_{\text{weft}}/\text{mm}$	$w_{\text{warp}}/\text{mm}$	$h_{\text{warp}}/\text{mm}$
Twill ($\gamma = 0^\circ$)	μ -CT	0.19 ± 0.03 ($\pm 16\%$)	0.19 ± 0.02 ($\pm 11\%$)	2.54 ± 0.14 ($\pm 6\%$)	0.21 ± 0.03 ($\pm 14\%$)	2.58 ± 0.25 ($\pm 10\%$)	0.22 ± 0.03 ($\pm 14\%$)
	2D scan	0.45 ± 0.04 ($\pm 9\%$)	0.27 ± 0.02 ($\pm 7\%$)	2.41 ± 0.19 ($\pm 8\%$)	2.64 ± 0.15 ($\pm 6\%$)		
Plain ($\gamma = 0^\circ$)	μ -CT	1.38 ± 0.08 ($\pm 6\%$)	0.45 ± 0.02 ($\pm 4\%$)	4.14 ± 0.25 ($\pm 6\%$)	0.54 ± 0.08 ($\pm 15\%$)	4.49 ± 0.21 ($\pm 5\%$)	0.53 ± 0.02 ($\pm 4\%$)
	2D scan	1.05 ± 0.37 ($\pm 35\%$)	0.61 ± 0.19 ($\pm 31\%$)	4.60 ± 0.27 ($\pm 6\%$)		4.33 ± 0.21 ($\pm 5\%$)	

Table 2
Experimental data and CFD predictions of in-plane permeability for different shear angles, γ : principal permeability values, K_1 and K_2 , and angle between K_1 and weft direction, θ ; average values, standard deviations and coefficients of variation (standard deviation/average) are given where appropriate.

		$K_1/10^{-10} \text{ m}^2$	$K_2/10^{-10} \text{ m}^2$	θ (°)	K_1/K_2
9-layer twill weave ($\gamma = 0^\circ$, $V_f = 0.40$)	Experiment	3.65 ± 0.44 ($\pm 12\%$)	2.24 ± 0.25 ($\pm 11\%$)	1 ± 14	1.65 ± 0.29 ($\pm 18\%$)
	Prediction	3.96 ± 0.51 ($\pm 13\%$)	2.50 ± 0.18 ($\pm 7\%$)	1 ± 5	1.59 ± 0.22 ($\pm 14\%$)
3-layer plain weave ($\gamma = 0^\circ$, $V_f = 0.51$)	Experiment	2.29 ± 0.76 ($\pm 33\%$)	1.41 ± 0.76 ($\pm 54\%$)	19 ± 37	1.74 ± 0.39 ($\pm 22\%$)
	Prediction	5.67 ± 1.39 ($\pm 25\%$)	0.80 ± 0.17 ($\pm 21\%$)	-1 ± 1	7.68 ± 3.43 ($\pm 45\%$)
3-layer plain weave ($\gamma = 10^\circ$, $V_f = 0.52$)	Experiment	1.63 ± 0.43 ($\pm 26\%$)	1.04 ± 0.27 ($\pm 26\%$)	-14 ± 28	1.57 ± 0.03 ($\pm 2\%$)
	Prediction	2.10 ± 0.85 ($\pm 40\%$)	0.94 ± 0.60 ($\pm 64\%$)	-14 ± 15	3.72 ± 1.11 ($\pm 30\%$)
3-layer plain weave ($\gamma = 20^\circ$, $V_f = 0.55$)	Experiment	1.32 ± 0.92 ($\pm 70\%$)	0.33 ± 0.17 ($\pm 51\%$)	-2 ± 6	3.80 ± 0.90 ($\pm 24\%$)
	Prediction	1.20 ± 0.24 ($\pm 20\%$)	0.51 ± 0.18 ($\pm 35\%$)	-22 ± 10	4.61 ± 6.24 ($\pm 17\%$)
3-layer plain weave ($\gamma = 25^\circ$, $V_f = 0.56$)	Experiment	0.80 ± 0.22 ($\pm 27\%$)	0.28 ± 0.07 ($\pm 27\%$)	-11 ± 10	2.88 ± 0.43 ($\pm 15\%$)
	Prediction	0.92 ± 0.35 ($\pm 38\%$)	0.26 ± 0.09 ($\pm 35\%$)	-17 ± 16	2.66 ± 1.10 ($\pm 41\%$)

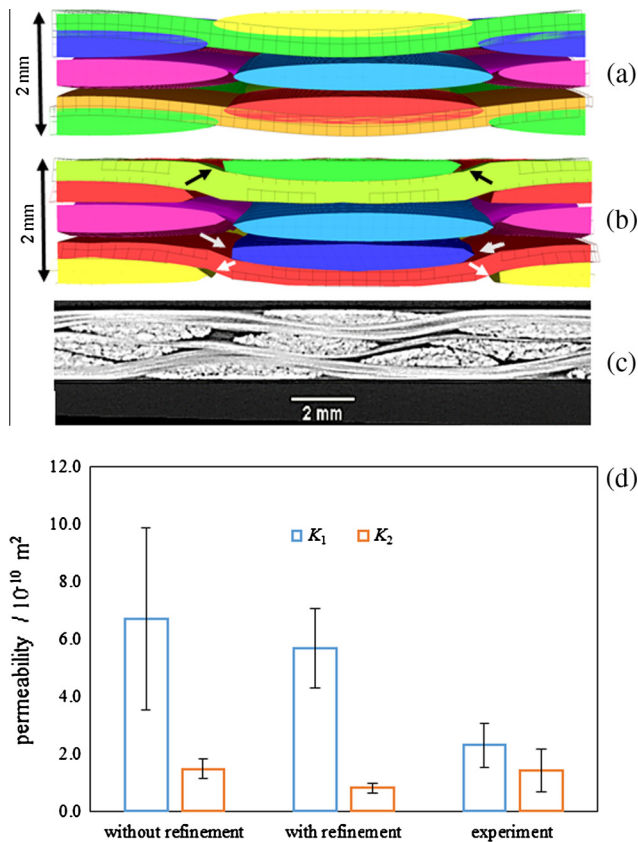


Fig. 10. Three layers of plain weave fabric: (a) TexGen model prior to any refinement to correct yarn intersections; (b) after the refinement; (c) μ -CT image of laminate cross-section; (d) CFD predictions based on six stochastic models and experimental results for K_1 and K_2 . (For interpretation of the references to colour in this figure legend, the reader is referred to the web version of this article.)

where A_1 and A_2 are derived from the experimentally determined permeability of the un-sheared fabric laminate (at $\gamma = 0^\circ$) and assumed to be constant. The fibre volume fraction, V_f , is a function of γ .

The angle θ is defined as the angle between the direction of the principal permeability, K_1 , and the weft yarns. An empirical equation between θ and the shear angle, γ , proposed by Endruweit and Ermanni [5] is used:

$$\theta = \frac{90^\circ - \gamma}{2} (1 - \sin^x(90^\circ - \gamma)), \text{ where } x = 5 \left(\left(\frac{K_1}{K_2} \right)_{\gamma=0^\circ} - 1 \right)^{-1} \quad (9)$$

Fig. 11 compares the analytical/empirical model in Eqs. (8) and (9) with CFD predictions and experimental data. For K_1 and K_2 (Fig. 11(a) and (b)), the decrease in permeability with increasing

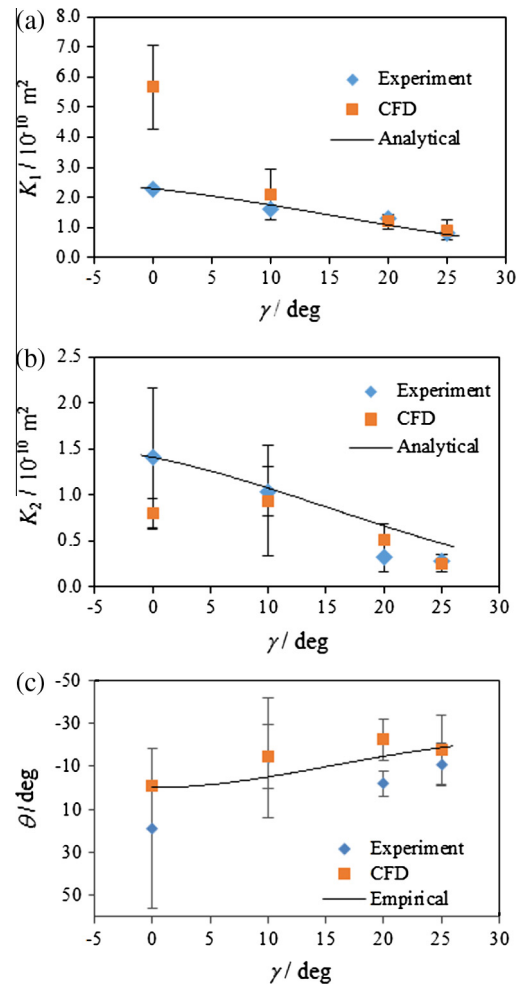


Fig. 11. Three layers of plain weave fabric: predicted permeability (K_1 , K_2 and θ) from CFD analysis as a function of the shear angle, together with experimental data and analytical/empirical predictions. (For interpretation of the references to colour in this figure legend, the reader is referred to the web version of this article.)

shear angle, indicated both by the CFD results and Eq. (8), is a result of superposition of the change in fibre volume fraction (described by the Kozeny–Carman equation) and the re-orientation of flow channels. This view is consistent with previous studies [1,2,5]. The numerical results predict experimental data generally with reasonable accuracy and follow the same trend as formulated in the analytical model in Eq. (8). Unlike the analytical model, the CFD simulations do not require calibration by experimental data of the un-sheared fabric ($\gamma = 0^\circ$). Hence, the numerical approach has

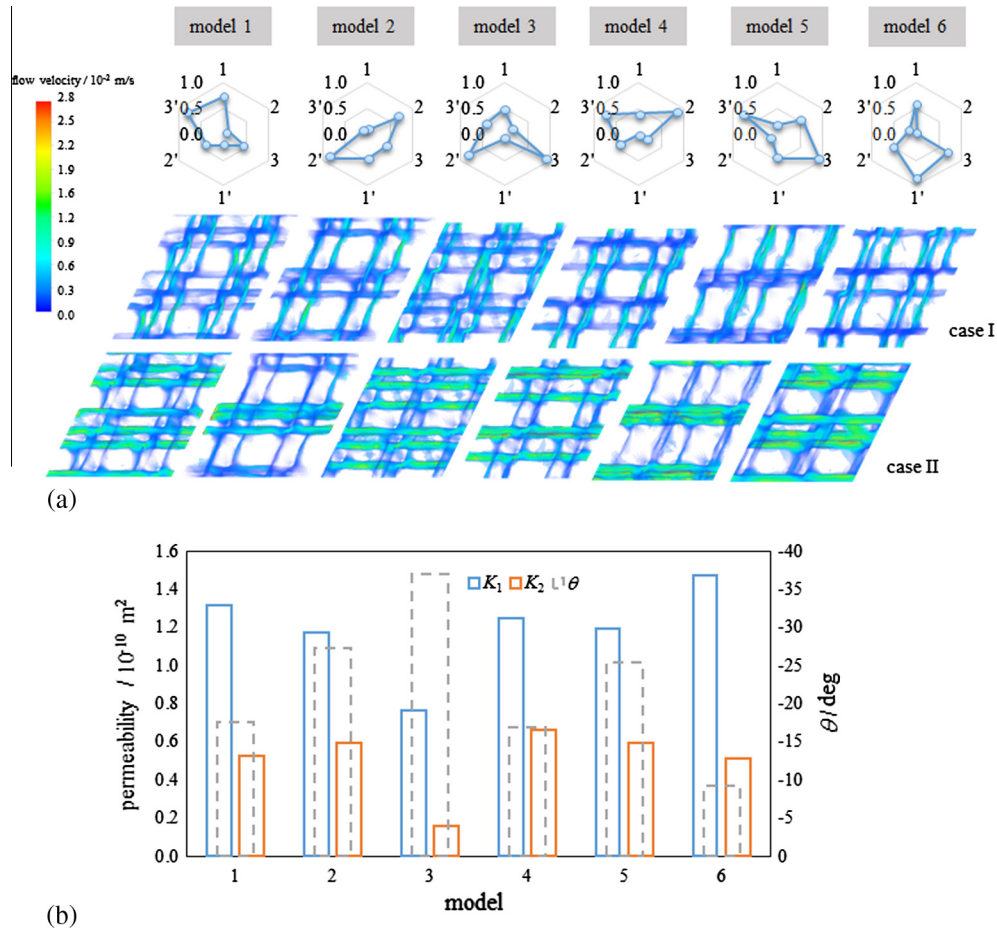


Fig. 12. (a) Top: radar charts of random in-plane shift for the 3-layer unit cell models; the radial axis (0–1) is the normalised shift over the unit cell dimensions in warp and weft directions, whilst each spoke represents each of 3 fabric layers being shifted in warp (1, 2, 3) and weft direction (1', 2', 3'); (a) bottom: resulting distributions of flow channels in the sheared plain weave fabric lay-up ($\gamma = 25^\circ$) due to the random shift, with predicted velocity field under the pressure boundary conditions case I and II as described in Section 3; (b): corresponding permeability predictions (K_1 , K_2 and θ) for the six stochastic models. (For interpretation of the references to colour in this figure legend, the reader is referred to the web version of this article.)

the advantage of being a truly predictive tool. Fig. 11(c) indicates that CFD predictions of the angle θ are in reasonable agreement with experimental data and the empirical model (Eq. (9)), which was deduced from experimental permeability data for different materials [5]. The data listed in Table 2 suggest that the scatter of the angle θ is related to the ratio of the major and minor axes of the flow front ellipse forming in radial flow, R_1/R_2 , which is equal to the square root of the ratio K_1/K_2 . The smaller the average K_1/K_2 , the more sensitive is the orientation of the flow front ellipse to small changes in the lay-up structure, e.g. caused by the random in-plane shift of fabric layers, which is discussed in the following section.

5.3. Prediction of permeability scatter

Characterising and predicting the variability of reinforcement permeabilities is a pre-requisite for robust design of LCM processes. For the fabric lay-ups in this study, standard deviations of experimental data and numerical predictions are listed in Table 2. Comparing data for unshredded fabrics, the permeability scatter for 9 layers of the twill weave fabric (experiment: up to $\pm 12\%$; prediction: up to $\pm 13\%$) is lower than for 3 layers of the plain weave fabric (experiment: up to $\pm 54\%$; prediction: up to $\pm 25\%$). With increasing number of layers, the effect of lay-up randomness on the permeability decreases. As reported by Lomov et al. [11], the distribution of the average thickness per layer becomes narrower,

and the average nesting configuration tends to converge when the number of layers increases. In addition, the influence of variations in the structure of individual layers (in actual specimens) on the permeability of the lay-up decreases with increasing number of layers. Numerical modelling, as illustrated in Fig. 12, enables a direct relation between the lay-up randomness, the flow channel distribution and the scatter of the permeability tensor to be derived. The flow channel distributions in Fig. 12 were visualised in ANSYS CFD-Post. For 3 layers of the plain weave fabric ($\gamma = 25^\circ$), the random in-plane shift of layers in warp and weft direction (Fig. 12(a), top) merges or separates the flow channels at each interface between layers. It is clear in Fig. 12(a) that model 6 has the most interconnected flow channels, whilst model 3 shows most isolated flow channels between fabric layers. The corresponding values of K_1 are $1.47 \times 10^{-10} \text{ m}^2$ for model 6 and $0.77 \times 10^{-10} \text{ m}^2$ for model 3 as show in Fig. 12(b). Similarly, K_2 for model 6 is 2.5 times that for model 3. The angle θ for model 3 is -37° , indicating that the orientation of K_1 rotates towards the warp direction. For model 6, $\theta = -9^\circ$ is closer to the weft direction.

6. Conclusion

This study presents a numerical approach for predicting permeabilities of deformed fabrics, which is based on geometrical data for un-deformed fabrics as input. Permeability values derived

from simulations of impregnating flow through fabric structures are not affected by operator-induced experimental issues and have the potential to be more reliable than experimental data, provided that numerical modelling is accurate. Starting from the undeformed fabric geometry, two levels of variation in material structure are modelled in TexGen to simulate realistic deformations of the lay-up material. The first level is related to yarn shape variation due to geometrical constraints imposed by shear and compression. The second level is related to stochastic variability in ply stacking. Comparison of permeability values predicted based on flow simulations using these detailed geometrical models with corresponding experimental data indicated an average difference of 10% for a twill weave fabric lay-up at $V_f = 0.40$ and an average difference of 20% for a plain weave fabric lay-up at different shear angles with $V_f > 0.52$. Considering that, unlike for existing analytical models, no calibration factor is required, the predictions show good accuracy, which also reflect that the refinement in geometrical modelling is more accurate for fabrics with low V_f . In addition, this study demonstrates that permeability scatter is closely related to the meso-scale geometry of fabric lay-ups.

Acknowledgements

This work was supported by the Engineering and Physical Sciences Research Council [grant number: EP/I033513/1], through the EPSRC Centre for Innovative Manufacturing in Composites. X-ray μ -CT was conducted at the Hounsfield Facility, School of Biosciences, University of Nottingham.

References

- Aranda S, Berg DC, Dickert M, Drechsel M, Ziegmann G. Influence of shear on the permeability tensor and compaction behaviour of a non-crimp fabric. *Compos Part B-Eng* 2014;65:158–63.
- Smith P, Rudd CD, Long AC. The effect of shear deformation on the processing and mechanical properties of aligned reinforcements. *Compos Sci Technol* 1997;57(3):327–44.
- Heardman E, Lekakou C, Bader MG. In-plane permeability of sheared fabrics. *Compos A Appl Sci Manuf* 2001;32(7):933–40.
- Louis M, Huber U. Investigation of shearing effects on the permeability of woven fabrics and implementation into LCM simulation. *Compos Sci Technol* 2003;63(14):2081–8.
- Endruweit A, Ermanni P. The in-plane permeability of sheared textiles. Experimental observations and a predictive conversion model. *Compos A Appl Sci Manuf* 2004;35(4):439–51.
- Verleye B, Croce R, Griebel M, Klitz M, Lomov S, Morren G, et al. Permeability of textile reinforcements: Simulation, influence of shear and validation. *Compos Sci Technol* 2008;68(13):2804–10.
- Merotte J, Simacek P, Advani SG. Flow analysis during compression of partially impregnated fiber preform under controlled force. *Compos Sci Technol* 2010;70(5):725–33.
- Endruweit A, Long AC. Analysis of compressibility and permeability of selected 3D woven reinforcements. *J Compos Mater* 2010;44(24):2833–62.
- Endruweit A, Matthys KS, Peiro J, Long AC. Effect of differential compression on in-plane permeability tensor of heterogeneous multi-layer carbon fibre preforms. *Plast, Rubber Compos* 2009;38(1):1–9.
- Grujicic M, Chittajallu KM, Walsh S. Effect of shear, compaction and nesting on permeability of the orthogonal plain-weave fabric preforms. *Mater Chem Phys* 2004;86(2–3):358–69.
- Lomov SV, Verpoest I, Peeters T, Roose D, Zako M. Nesting in textile laminates: geometrical modelling of the laminate. *Compos Sci Technol* 2003;63(7):993–1007.
- Hoes K, Dinescu D, Sol H, Parnas RS, Lomov S. Study of nesting induced scatter of permeability values in layered reinforcement fabrics. *Compos A Appl Sci Manuf* 2004;35(12):1407–18.
- Endruweit A, Zeng X, Long AC. Effect of specimen history on structure and in-plane permeability of woven fabrics. *J Compos Mater* 2014. 0021998314536070.
- Arbter R, Beraud J, Binetruy C, Bizet L, Bréard J, Comas-Cardona S, et al. Experimental determination of the permeability of textiles: a benchmark exercise. *Compos A Appl Sci Manuf* 2011;42(9):1157–68.
- Vernet N, Ruiz E, Advani S, Alms JB, Aubert M, Barbarski M, et al. Experimental determination of the permeability of engineering textiles: Benchmark II. *Compos Part a-Appl S* 2014;61:172–84.
- Nedanov PB, Advani SG. Numerical computation of the fiber preform permeability tensor by the homogenization method. *Polym Compos* 2002;23(5):758–70.
- Chen Z-R, Lin Ye, Meng Lu. Permeability predictions for woven fabric preforms. *J Compos Mater* 2010;44(13):1569–86.
- Song Y. Prediction of permeability tensor for three dimensional circular braided preform by applying a finite volume method to a unit cell. *Compos Sci Technol* 2004;64(10–11):1629–36.
- Loix F, Badel P, Orgéas L, Geindreau C, Boisse P. Woven fabric permeability: from textile deformation to fluid flow mesoscale simulations. *Compos Sci Technol* 2008;68(7–8):1624–30.
- Green SI, Wang Z, Waung T, Vakili A. Simulation of the flow through woven fabrics. *Comput Fluids* 2008;37(9):1148–56.
- Liu HL, Hwang WR. Permeability prediction of fibrous porous media with complex 3D architectures. *Compos A Appl Sci Manuf* 2012;43(11):2030–8.
- Lin H, Zeng X, Sherburn M, Long AC, Clifford MJ. Automated geometric modelling of textile structures. *Text Res J* 2012;82(16):1689–702.
- Sherburn M. Geometric and mechanical modelling of textiles [PhD Thesis]; University of Nottingham; 2007.
- McKay MD, Beckman RJ, Conover WJ. Comparison of three methods for selecting values of input variables in the analysis of output from a computer code. *Technometrics* 1979;21(2):239–45.
- Olsson AMJ, Sandberg GE. Latin hypercube sampling for stochastic finite element analysis. *J Eng Mech-Asce* 2002;128(1):121–5.
- Jiang D, Li Y, Fei Q, Wu S. Prediction of uncertain elastic parameters of a braided composite. *Compos Struct* 2015(0).
- Gebart BR. Permeability of unidirectional reinforcements for Rtm. *J Compos Mater* 1992;26(8):1100–33.
- Grouve WJ, Akkerman R. An idealised BC for the meso scale analysis of textile impregnation. The 9th international conference on flow processes in composite materials. Montreal 2008.
- Advani SG, Sozer EM. Process modeling in composites manufacturing. CRC Press; 2002.
- Vanaerschot A, Cox BN, Lomov SV, Vandepitte D. Stochastic framework for quantifying the geometrical variability of laminated textile composites using micro-computed tomography. *Compos A Appl Sci Manuf* 2013;44:122–31.
- Gan J, Bickerton S, Battley M. Quantifying variability within glass fibre reinforcements using an automated optical method. *Compos A Appl Sci Manuf* 2012;43(8):1169–76.
- Endruweit A, McGregor P, Long AC, Johnson MS. Influence of the fabric architecture on the variations in experimentally determined in-plane permeability values. *Compos Sci Technol* 2006;66(11–12):1778–92.
- Long AC, Rudd CD, Blagdon M, Smith P. Characterizing the processing and performance of aligned reinforcements during preform manufacture. *Compos Part A: Appl Sci Manuf* 1996;27(4):247–53.